Journal of Analysis and Testing (2025) 9:301–310
https://doi.org/10.1007/s41664-025-00374-x

ORIGINAL PAPER

Electrochemiluminescence of Hot Exciton Nanomaterial Featuring Aggregation-Induced Emission for "Signal-on" Detection of Alkaline Phosphatase

Zhiwei Tang[1] · Chunlan Li[2] · Chao Wang[1] · Mengchen Wang[1] · Huangxian Ju[1]

Received: 31 March 2025 / Accepted: 21 April 2025 / Published online: 9 June 2025

Abstract
Traditional fluorescent emitters cannot effectively utilize triplet excitons owing to the spin statistical limitation, thus their electrochemiluminescence (ECL) efficiency (Φ_{ECL}) is relatively low. Improving the utilization efficiency of triplet excitons is of great significance for developing efficient luminescent materials. Here we designed a hot exciton molecule (NZ2TPA) containing highly efficient chromophore naphthothiadiazole as an electron acceptor and triphenylamine (TPA) with aggregation induced emission (AIE) property as the strong electron donor to synthesize an ECL nanoemitter-NZ2TPA nanoparticles (NT NPs). The hybridized local and charge-transfer (HLCT) excited state of NZ2TPA achieved a high exciton utilization through the reverse intersystem crossing from higher triplet states (*h*RISC). The combination of HLCT and AIE characteristics endowed NT NPs with superior Φ_{ECL} over other nanoemitters, which provided an excellent material for the design of highly sensitive ECL biosensors. Using alkaline phosphatase (ALP) as an analyte model, a "signal-on" ECL biosensing approach was constructed by combining the quenching of manganese dioxide nanosheets (MnO_2 NSs) on ECL emission of NT NPs and the reduction of MnO_2 by ascorbic acid produced from ALP-catalyzed dephosphorylation, which showed a detectable range of 0.004 − 400 U/L with a detection limit of 0.57 mU/L. The excellent performance demonstrated the immense potential of organic nanomaterials through combining HLCT and AIE properties to improve Φ_{ECL}.

Keywords Electrochemiluminescence · Organic nanomaterials · Hot exciton · Hybridized local and charge-transfer · Aggregation induced emission · Alkaline phosphatase

1 Introduction

Electrochemiluminescence (ECL) is a phenomenon where the luminophore undergoes redox processes on the electrode surface to generate excited states, and then emits light through radiation relaxation [1–4]. It has become a reliable analytical method [5–7] for its low background signal [8, 9] and excellent spatial–temporal controllability [10]. Compared with traditional ECL materials, such as $Ru(bpy)_3^{2+}$ [11, 12] and quantum dots [13, 14], the organic luminescent materials possess low toxicity, adjustable structure and better biocompatibility [15, 16]. Thus, a lot of works have been reported to modify the structure of organic compounds to acquire special properties [17–20]. Our previous work enhanced the luminescent efficiency of polymer dots (Pdots) by introducing cyano group as electron acceptor into polymer [17]. By covalently linking triethylamine to polymer chain, we further developed coreactant-embedded Pdots to propose a dual intramolecular electron transfer strategy for enhancing the ECL efficiency (Φ_{ECL}) [18]. Xu et al. designed an aggregation-induced ECL emitter by connecting benzo-bis(1,2,5-thiadiazole) and tetraphenylethylene with alkyl thiophene as a π-bridge [19]. Wu et al. then enhanced the luminescence efficiency through highly twisted molecular conformation and efficient intramolecular charge transfer effect [20]. However, owing to the spin statistical limitation, only the lowest singlet excitons (S_1) in fluorescent organic

✉ Huangxian Ju
hxju@nju.edu.cn

[1] State Key Laboratory of Analytical Chemistry for Life Science, School of Chemistry and Chemical Engineering, Nanjing University, Nanjing 210023, China

[2] Henan Key Laboratory of Biomolecular Recognition and Sensing, Henan Joint International Research Laboratory of Chemo/Biosensing and Early Diagnosis of Major Diseases, College of Chemistry and Chemical Engineering, Shangqiu Normal University, Shangqiu 476000, China

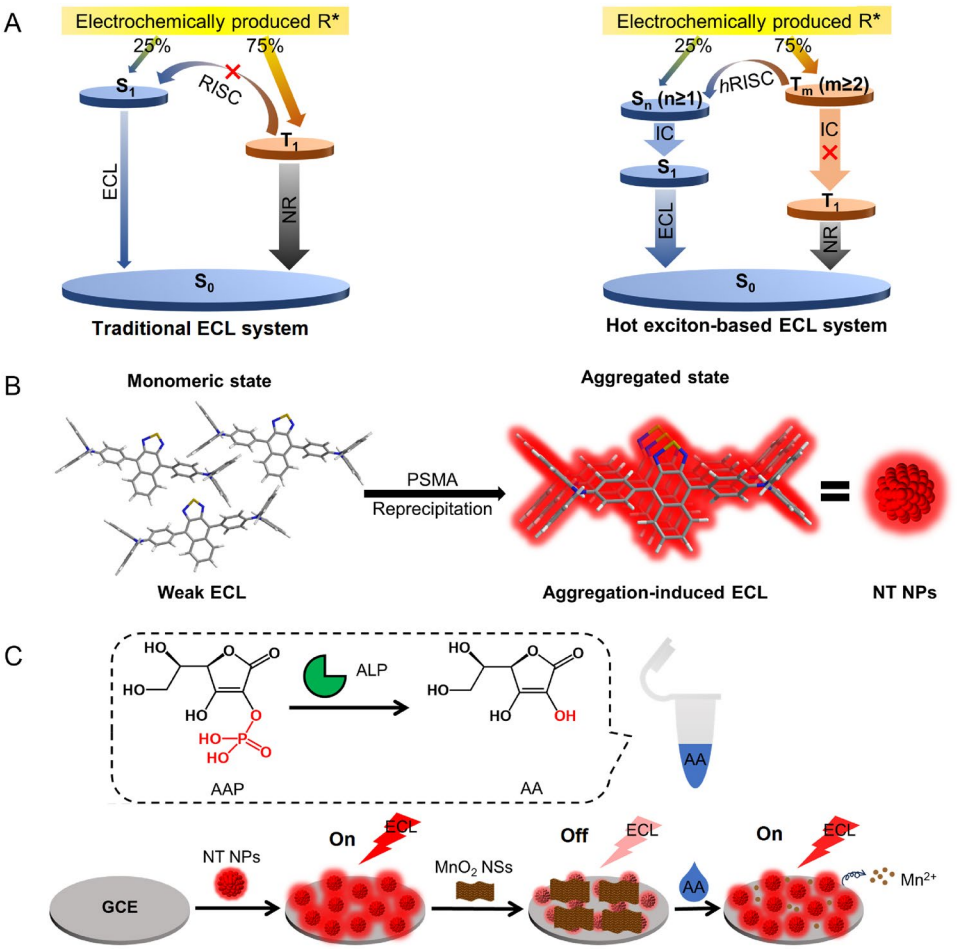

Scheme 1 Schematic diagrams of **A** traditional and hot exciton-based ECL systems [29], **B** NT NPs preparation, and **C** fabrication of ECL biosensor for ALP detection

emitters can generate ECL emission via radiative transition after electrochemical excitation [21], while the lowest triplet excitons (T_1) cannot emit ECL due to the transition prohibition (Scheme 1A, left), thus the maximum Φ_{ECL} is estimated to be only 25% for conventional organic nanomaterials [21].

The organic nanomaterials exhibiting thermally activated delayed fluorescence (TADF) properties have demonstrated the effective utilization of triplet excitons [22–24] through reverse intersystem crossing (RISC) from T_1 to S_1 owing to the sufficiently small energy bandgap (ΔE_{ST}) between S_1 and T_1 states of TADF molecules (≈ 0.1 eV) [25]. For example, our recent work fabricated TADF Pdots using the sterically locked electron donor–acceptor (D-A) polymer to yield an anodic Φ_{ECL} of 49.9% relative to $Ru(bpy)_3^{2+}$ [26]. Nevertheless, the spatial separation of orbitals forbids electronic transition and thus limits the luminous efficiency [27], and long-lived T_1 excitons also cause exciton annihilation through the accumulation process [28]. To address this issue, we further designed a hot exciton molecule with hybridized local and charge-transfer (HLCT) excited state property [29] to achieve the RISC from high-lying triplet states (*h*RISC) to singlet states ($T_m \rightarrow S_n$, $m \geq 2$, $n \geq 1$) [29, 30] and inhibit the internal conversion (IC) of T_m to T_1 for reducing the accumulation of T_1 excitons [31–33] (Scheme 1A, right), which could enhance both the luminous efficiency and the exciton utilization [34, 35].

This work used naphtho[2,3-c][1,2,5]thiadiazole (NZ) as an electron acceptor and triphenylamine (TPA) with aggregation induced emission (AIE) property as an strong electron donor to synthesize a hot exciton molecule, 4,4'-(naphtho[2,3-c][1,2,5]thiadiazole-4,9-diyl)bis(N,N-diphenylaniline) (NZ2TPA), through a Suzuki coupling reaction [36], and then NZ2TPA nanoparticles (NT NPs) by reprecipitation (Scheme 1B). The solvatochromic experiments and simulation calculations demonstrated the HLCT character of NZ2TPA. The presence of AIE greatly enhanced the ECL emission of NZ2TPA after reprecipitation. Thus the NT NPs generated intense anodic ECL emission with a high Φ_{ECL} of 62.7% *vs.* $Ru(bpy)_3^{2+}$ in the presence of coreactant tripropylamine (TPrA). To verify the analytical application, we further used alkaline phosphatase (ALP) as an analyte model and manganese dioxide nanosheets (MnO_2 NSs) as an ECL quencher to propose a simple "signal-on" method based on the reduction of MnO_2 on biosensor surface by ascorbic acid produced from ALP-catalyzed dephosphorylation of ascorbic acid

2-phosphate (AAP). The outstanding performance of the proposed method highlighted the promising application of organic nanomaterials with AIE and HLCT dual functional characteristics as efficient ECL emitters.

2 Experimental

2.1 Preparation of Aggregates for Fluorescent and ECL Analysis

The solutions of aggregates at different water contents were prepared by adding tetrahydrofuran (THF) solution of NZ2TPA (2 mM, 0.1 mL) to the mixtures of THF/H_2O (2.9 mL, with appropriate ratios) to sonicate for 5 min, which were used for fluorescent and ECL measurements.

2.2 Preparation of NT NPs

NT NPs were prepared by the reprecipitation method [37]. Briefly, a 2.5 mL mixture of 50 μg/mL NZ2TPA and 10 μg/mL poly(styrene-co-maleic anhydride) (PSMA) in THF was rapidly injected into 10 mL water after ultrasonic degassing for 20 min and followed by ultrasonic treatment lasting 10 s. The THF was subsequently eliminated via rotary evaporation under vacuum, and the NT NPs dispersion was ultimately obtained by filtration through a 0.22 μm poly(ether sulfones) filter.

2.3 Synthesis of MnO_2 NSs

The synthesis of MnO_2 NSs was performed according to previous reports [38]. Typically, 1 mL of 15 mM $KMnO_4$ was added to 2 mL of 50 mM pH 6.0 2-(N-morpholino) ethanesulfonic acid (MES), followed by dilution to a total volume of 10 mL. The mixture was then ultrasonicated for about 30 min to obtain MnO_2 NSs after centrifugation at 10,000 r/min for 15 min. After triple washing with deionized water, the MnO_2 NSs were dispersed with 10 mL of deionized water and stored in a refrigerator at 4 ℃. The concentration of the MnO_2 NSs dispersion was 0.16 mg/mL [39].

2.4 Fabrication of ECL Biosensor

A glassy carbon electrode (GCE, 5 mm in diameter) was polished with 0.05 μm alumina slurry and then sonicated in alternating ethanol and water. After drying with N_2, NT NPs modified were prepared by dropping 20 μL NT NPs aqueous solution on the surface and dried at 37 ℃ for 1 h. To prepare the ECL biosensor, 20 μL of 0.16 mg/mL MnO_2 NSs was drop-cast onto NT NPs/GCE and dried at 37 ℃ for 1 h to form MnO_2 NSs/NT NPs/GCE.

2.5 Procedure for ALP Detection

400 μL of 10 mM Tris-HCl buffers (pH 8.0) containing different concentrations of ALP and 20 mM AAP were incubated at 37 ℃ for 60 min. Then, the MnO_2 NSs/NT NPs/GCEs were immersed in the reactant solution at room temperature for 4 min, rinsed with water and dried with N_2 for further ECL testing.

2.6 ECL Measurement

The ECL measurement was conducted in 0.1 M pH 7.4 phosphate buffer saline (PBS) with 20 mM TPrA with potential scanning from 0 to + 1.5 V. Scan rate: 100 mV/s. PMT: 500 V. The ECL intensity variation was represented by ΔI ($\Delta I = I - I_0$), where I_0 represents the ECL signal of MnO_2 NSs/NT NPs/GCE and I represents the ECL signal of MnO_2 NSs/NT NPs/GCE treated with the product of ALP-catalyzed dephosphorylation of AAP.

3 Results and Discussion

3.1 Molecular Structure and Photophysical Properties of NZ2TPA

The successful synthesis of NZ2TPA (Scheme S1) was confirmed by NMR and mass spectrometry (Fig. S1-S3). After optimizing the molecular structure, the freely rotating phenyl ring structure of the TPA unit avoided the fluorescence (FL) quenching induced by intermolecular accumulation. The angle between the central acceptor and the adjacent phenyl ring was 57° (Fig. S4), resulting in a large twisted structure of the molecule, which was conducive to the formation of the charge transfer (CT) state [40]. The UV–vis absorption and fluorescence (FL) spectra of NZ2TPA were measured in various polar solvents (Fig. 1A, B, Table S1). The UV–vis absorption near 520 nm was ascribed to the intramolecular charge transfer (ICT) transition from the TPA unit to the NZ unit. The shape and location of the absorption peak exhibited negligible variations in various solvents. As the polarity of solvents strengthened, the FL spectra of NZ2TPA gradually broadened with a total redshift of 47 nm, suggesting that NZ2TPA showed an obvious solvatochromic effect, and the excited state of S_1 possessed a certain CT state character [40].

To further understand the excited state property of NZ2TPA, the dipole moment of the excited state S_1 of NZ2TPA was investigated through the dependence of Stokes shift (ν_a-ν_f) on orientation polarization (Δf) according to the Lippert-Mataga model [41, 42]. Two fitting curves revealed that the dipole moment of NZ2TPA was small in low polar solvents and larger in higher polar solvents, corresponding to

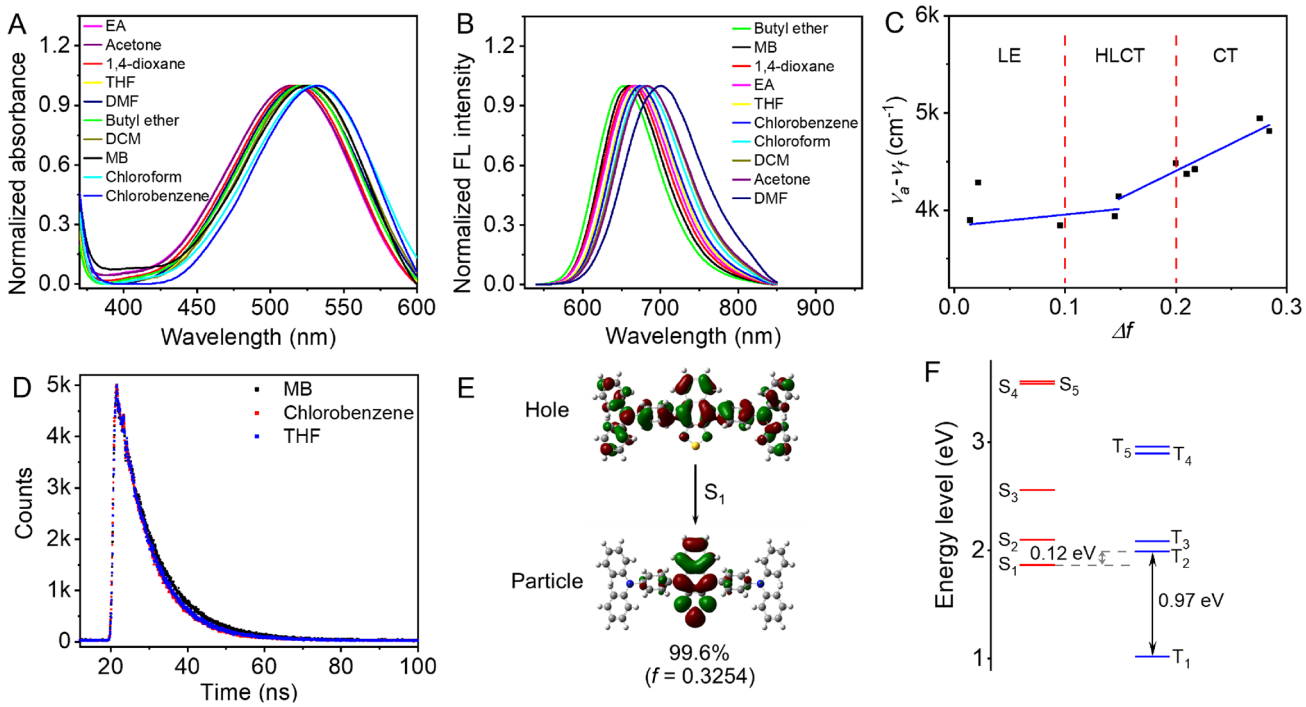

Fig. 1 **A** Normalized UV–vis absorption and **B** FL spectra of NZ2TPA in different solvents. **C** The plot of Stokes shift (ν_a-ν_f) *vs.* orientation polarization (Δf) of solvent for NZ2TPA. **D** Transient photoluminescence decay spectra of NZ2TPA in different solvents. **E** Natural transition orbitals of $S_1 \rightarrow S_0$ (*f* represents the oscillator strength, and the percentage indicates the transition possibility). **F** Energy levels of the first five singlet and triplet excited states in NZ2TPA

the dominance of the locally excited (LE) and CT states in the S_1 state (Fig. 1C), respectively. In medium polarity solvents, the S_1 state displayed both LE and CT characteristics. In addition, the transient fluorescence spectra of NZ2TPA in three representative solvents (toluene, trichloromethane and tetrahydrofuran) was 9.76 ns, 8.48 ns and 8.74 ns, respectively (Fig. 1D), showing a single exponential fitting decay, indicating that the S_1 state of NZ2TPA was a hybrid state combining LE and CT characteristics, without clear separation between two states [43].

Furthermore, the HLCT characteristic of NZ2TPA was confirmed through theoretical calculations at the molecular structure and orbital distribution level. The natural transition orbitals (NTOs) from $S_0 \rightarrow S_1$ excitation showed the particles primarily located on the NZ acceptor and its adjacent phenyl rings, and the holes distributed throughout the molecular structure (Fig. 1E), indicating that the $S_0 \rightarrow S_1$ transition contained both the LE characteristics of the NZ unit and the CT characteristics from the TPA unit to the NZ unit. The energy level diagrams showed that the energy gap between T_2 and T_1 (0.97 eV) was much larger than that between T_2 and S_1 (0.12 eV) (Fig. 1F, Table S2), indicating that the *h*RISC process from T_2 to S_1 was more preferable than the IC process from T_2 to T_1 according to the energy-gap law [44]. This was also consistent with the hot excitons mechanism to achieve a high utilization of triplet excitons.

To verify the AIE property of NZ2TPA, FL spectra of NZ2TPA in different ratios of THF/H_2O mixtures were measured (Fig. 2A). When the water volume fraction (f_w) increased, the FL spectra of NZ2TPA presented a slight redshift with the rapid decrease in intensity to its minimum at the f_w of 40%. This change was attributed to the twisted intramolecular charge transfer (TICT) effect. The FL emission increased from the f_w of 50% and reached a maximum at the f_w of 90% (Fig. 2B), demonstrating obvious AIE properties. Moreover, after NZ2TPA-THF/H_2O solutions with different f_w were cast on the GCE surface, the ECL intensity in 0.1 M pH 7.4 PBS with 20 mM TPrA.

As coreactant increased with the increasing f_w (Fig. 2C, D), revealing that the aggregation of NZ2TPA could enhance its ECL emission.

3.2 Synthesis and Characterization of NT NPs

NT NPs prepared by reprecipitation exhibited a spherical morphology with a diameter of about 21 nm (Fig. 3A, B). Dynamic light scattering (DLS) analysis of NT NPs showed a mean hydrodynamic diameter of 29 nm (Fig. 3C), slightly larger than the result of atomic force microscope (AFM). The dispersion was purplish-red in daylight and red upon 365 nm UV excitation (inset in Fig. 3D). The UV absorption spectrum of the THF

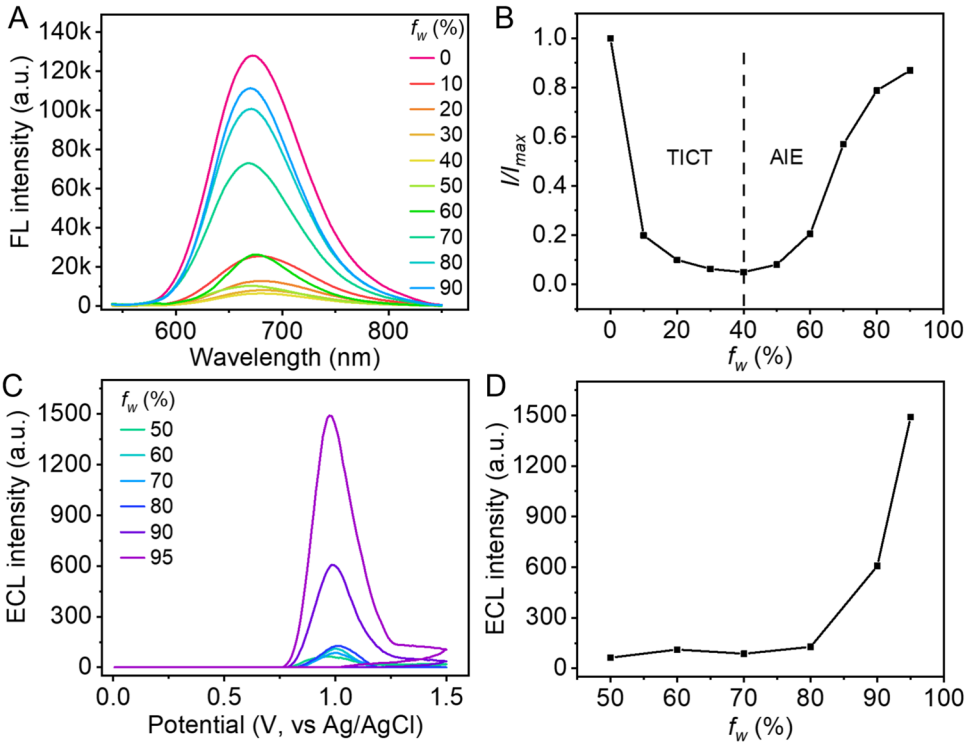

Fig. 2 **A** FL spectra of NZ2TPA in THF/H_2O mixtures with different water fractions (f_w). **B** The plot of I (emission intensity)/I_{max} (emission intensity in THF solution) of NZ2TPA *vs.* f_w. **C** ECL-potential curves of GCEs modified with 10 μL NZ2TPA in THF/H_2O mixtures with different water fractions in 0.1 M pH 7.4 PBS containing 20 mM TPrA. **D** The plot of ECL intensity *vs.* f_w

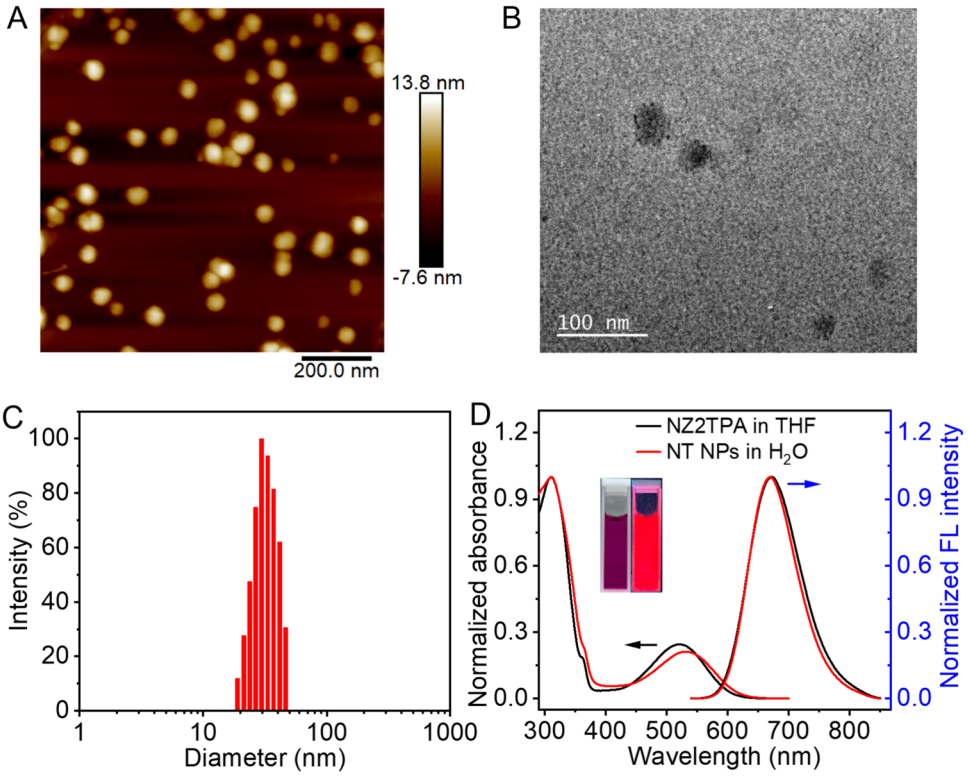

Fig. 3 **A** AFM and **B** TEM images of NT NPs. **C** The hydrodynamic diameter of NT NPs measured using DLS. **D** Normalized UV–vis absorption and FL spectra of NZ2TPA and NT NPs (insets: photographs of NT NPs dispersion under daylight (left) and 365 nm irradiation (right))

solution of NZ2TPA exhibited two absorption peaks at 310 and 521 nm (Fig. 3D). The former originated from π-π* interaction, and the latter resulted from ICT. The absorption of NT NPs in water at 532 nm showed a redshift of 11 nm due to the interactions between NPs and the surrounding solvent environment, reducing the energy required for the electronic transition [45].

The FL emission peak of NT NPs at 673 nm overlapped with that of NZ2TPA in THF, indicating NT NPs inherited the photophysical properties from NZ2TPA.

3.3 Electrochemical and ECL Behaviors of NT NPs

In N_2-saturated 0.1 M pH 7.4 PBS, the cyclic voltammogram (CV) of NT NPs/GCE showed an obvious irreversible oxidation peak at + 1.20 V and a weak reduction peak near − 1.7 V (Fig. 4A). The direction of potential scanning hardly affected the redox processes. However, two different directions led to obviously different annihilation of ECL emissions. Compared with the ECL emission at + 0.8 V during the potential scanning from 0 to + 1.5 V and then − 2.0 V (Fig. 4B, curve a), the potential scanning from 0 to − 2.0 V and then + 1.5 V led to two ECL peaks at − 2.0 V and + 0.94 V, respectively (Fig. 4B, curve b), indicating the electroreduction state of NT NPs (NT $NPs^{\bullet-}$) retained sufficient stability to undergo annihilation ECL emission with subsequent.

Moreover, the transient ECL revealed that the ECL emission was only generated at + 1.5 V when the potential stepped from − 2.0 V to + 1.5 V (Fig. 4C). Additionally, the ECL intensity of this potential step was greater than that of from + 1.5 V to − 2.0 V (Fig. 4C, D), which further confirmed the stability of NT $NPs^{\bullet-}$ [17]. The emission process of ECL annihilation was expressed by the Eqs. 1 − 4:

$$\text{NT NPs} + e^- \rightarrow \text{NT NPs}^{\cdot-} \quad (1)$$

$$\text{NT NPs} - e^- \rightarrow \text{NT NPs}^{\cdot+} \quad (2)$$

$$\text{NT NPs}^{\cdot+} + \text{NT NPs}^{\cdot-} \rightarrow \text{NT NPs}^* \quad (3)$$

$$\text{NT NPs}^* \rightarrow \text{NT NPs} + hv \quad (4)$$

Using TPrA as an optimal coreactant (Fig. S5a), which exhibited an irreversible oxidation with an onset potential of + 0.65 V and a peak at + 0.97 V (Fig. 5A, curve a), the anodic ECL emission of NT NPs/GCE at an optimized concentration of 20 mM (Fig. S5b) was studied. In the absence of TPrA, the oxidation of NT NPs in PBS showed an onset potential of + 0.51 V with an anodic peak at + 1.21 V (Fig. 5A, curve b). Upon the addition of TPrA in PBS, NT NPs/GCE displayed the anodic peaks of both TPrA and NT NPs at the same potentials as the oxidation of TPrA and NT NPs (Fig. 5A, curve c), and a prominent ECL emission peak occurred at + 0.91 V with an onset potential at + 0.71 V (Fig. 5B, curve c), more positive than the onset potentials for the oxidation of both TPrA and NT NPs, indicating that the ECL emission originated from the excited species NT NPs^* generated by the reaction between oxidized TPrA and NT NPs, $TPrA^{\bullet}$ and $NPs^{\bullet+}$ [46]. The relatively lower ECL peak potential than the oxidation peak of NT NPs could be attributed to the ICT resulting from the twisted molecular structure [20]. The intense ECL emission arose from the transition of the triplet excitons to the singlet state via *h*RISC (Scheme 1; [29]; Fig. 5C), which could not be observed in

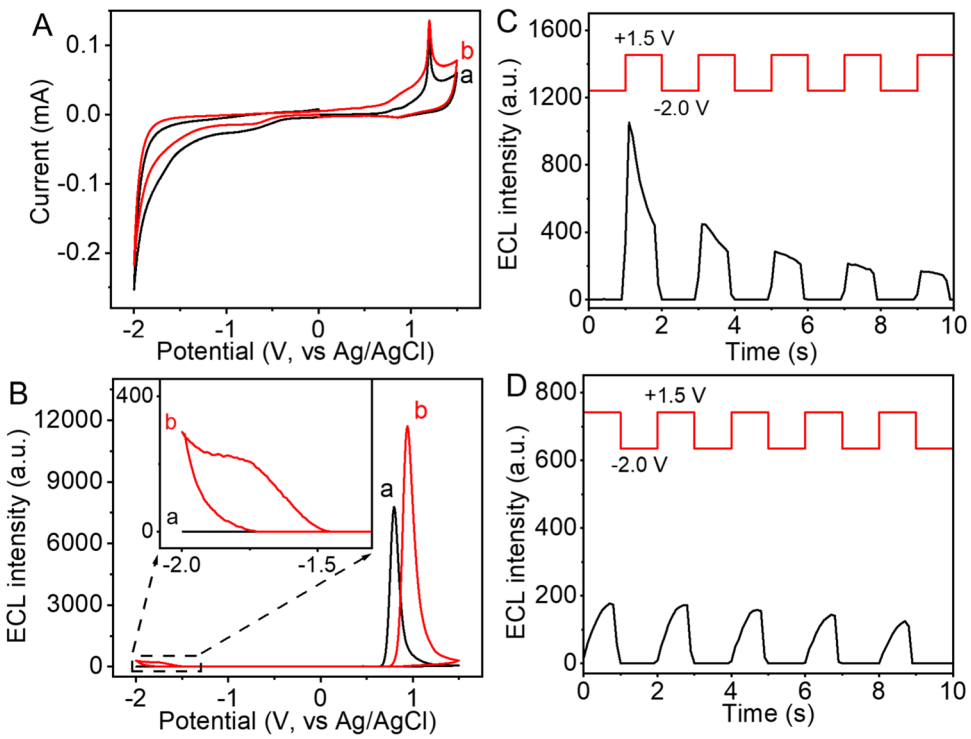

Fig. 4 **A** CV and **B** ECL curves of NT NPs/GCE in N_2-saturated 0.1 M pH 7.4 PBS (curve a) from 0 to + 1.5 V and then − 2.0 V, and (curve b) from 0 to − 2.0 V and then + 1.5 V. Scan rate: 100 mV/s. PMT: 700 V. **C**, **D** ECL transients of NT NPs/GCE in N_2-saturated 0.1 M pH 7.4 PBS with steps from **C** − 2.0 V to + 1.5 V and **D** + 1.5 V to − 2.0 V

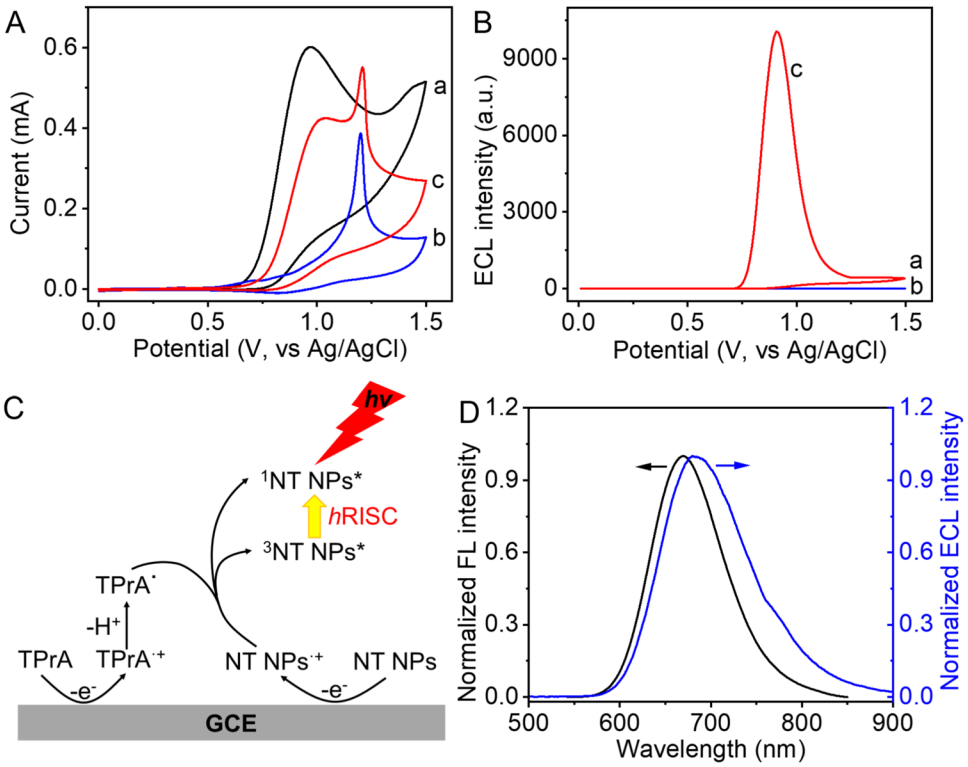

Fig. 5 **A** CV and **B** ECL curves of bare (curve a) and NT NPs modified (curves b, c) GCE in 0.1 M pH 7.4 PBS in the absence (curve b) and presence (curves a, c) of 20 mM TPrA. Scan rate: 100 mV/s. PMT: 450 V. **C** Anodic ECL mechanism of NT NPs in the presence of TPrA. **D** Normalized FL spectrum of NT NPs dispersion and ECL spectrum of NT NPs/GCE in 0.1 M pH 7.4 PBS containing 20 mM TPrA

very weak cathodic ECL emission of NT NPs with 20 mM $K_2S_2O_8$ as a cathodic coreactant (Fig. S6, curves 3). Compared with NT NPs/GCE, NZ2TPA/GCE exhibited much weaker anodic ECL emission (Fig. S7a and b), indicating that NT NPs synthesized by reprecipitation could enhance the stability of organic molecules and avoid the interference of dissolved oxygen in water, thereby improving the ECL intensity of the designed nanomaterial.

The ECL spectrum of NT NPs showed a wide emission peak at around 680 nm (Fig. 5D) that red-shifted by 10 nm compared with its FL emission peak, which might be attributed to the influence of instrument error [47]. The nearly matched spectra suggested that the ECL emission of NT NPs was a band-gap model [48].

From the CV curves of NT NPs/GCE in non-aqueous phase measured using ferrocene as the internal standard (Fig. S8a and b) and their initial oxidation/reduction potentials, the HOMO and LUMO of NT NPs were determined to be − 5.23 eV and − 3.63 eV, respectively, and the energy gap (E_g) was calculated to be 1.60 eV (Table S3), slightly smaller than the theoretically calculated energy gap of 2.24 eV (Fig. S8c), indicating the semiconductor property of NT NPs. Using 1 mM $Ru(bpy)_3^{2+}$ as the standard, the anodic ECL efficiency of NT NPs was calculated to be 62.7% at 10 mM TPrA (Fig. S9a and b, Table S4) [18], which was 5.6 times higher than 11.2% of CN-PPV dots [17] and greater than 56.7% of the hot exciton materials (BCzP-BT nanorods) [29] (Table S5), even similar to that of the TADF aggregates [49], showing the significance combining the HLCT with AIE properties in boosting the ECL efficiency. In addition, the ECL intensity of NT NPs over various storage periods with a relative standard deviation (RSD) of 5.9% confirmed its excellent storage stability (Fig. S10).

3.4 Analytical Application of NT NPs in ECL Detection

Using ALP, a hydrolase widely present in mammalian tissues and directly related to hepatobiliary disease, bone diseases, and diabetes [50], as an analyte target, an "on–off-on" ECL detection method was constructed by using NT NPs as an efficient anodic ECL emitter and MnO_2 NSs to quench the ECL signal of NT NPs [51] (Scheme 1C). When the substrate AAP was catalytically hydrolyzed by ALP to remove phosphate, the generated AA could reduce MnO_2 NSs to Mn^{2+} to recover the ECL emission.

The prepared MnO_2 NSs were characterized with TEM images, UV absorbance and X-ray photoelectron spectroscopy (XPS). The TEM images of the prepared MnO_2 NSs showed obvious nanosheet morphology and a unique UV absorbance band near 380 nm (Fig. S11a and b). Two characteristic peaks of the XPS spectrum at 642.2 and 653.8 eV were related to Mn $2p_{3/2}$ and Mn $2p_{1/2}$ (Fig. S11c) [52], respectively. After MnO_2 NSs being cast on NT NPs/GCE, the electrochemical impedance spectra (EIS) showed a significantly decrease in electron-transfer resistance

(R_{et}) (Fig. S12a), but the ECL emission greatly decreased (Fig. S12b), while the CV curves did not show obvious difference from those in the absence of MnO_2 NSs (Fig. S12c and Fig. 5A), indicating that the presence of MnO_2 NSs on NT NPs/GCE did not affect the oxidation of both NT NPs and TPrA except the accelerated electron transfer and that the great ECL decrease of NT NPs resulted from the quenching of MnO_2 NSs. The quenching effect could be verified through the partial overlap between the ECL spectrum of NT NPs and the UV–vis spectrum of MnO_2 NSs (Fig. S12d), which was inferred from their ECL resonance energy transfer [53]. After treating MnO_2 NSs/NT NPs/GCE with AA produced by ALP-catalyzed dephosphorylation of AAP, the dissolution of MnO_2 NSs led to the increase of R_{et} due to the poor conductivity of NT NPs (Fig. S12a, curve 2) and the recovery of ECL emission (Fig. S12a and b, curves 4), demonstrating the feasibility to detect the ALP activity.

To achieve the sensitive detection of ALP, the amount of MnO_2 NSs for biosensor preparation, the concentration of AAP and pH for ALP-catalyzed dephosphorylation, and the reaction time for the dissolution of MnO_2 NSs were optimized to 0.16 mg/mL, 20 mM, pH 8.0 and 4 min, respectively (Fig. S13). Under the optimal conditions, the ECL signal increased with the increasing ALP concentration (Fig. 6A). The ECL intensity exhibited an excellent linear correlation with the logarithm of ALP concentration over a range of 0.004−400 U/L (Fig. 6B). The detection limit was estimated at a signal-to-noise ratio of 3 to be 0.57 mU/L. Both the detectable activity range was much wider and the detection limit was much lower than those of previously reported colorimetric, fluorescent and ECL methods (Table S6), displaying the advantage of the proposed hot exciton nanomaterial with strong ECL emission and high ECL efficiency.

The selectivity of the biosensor was verified by comparing the ECL response of several interfering enzymes, including glucose oxidase, catalase, lysozyme, and pepsin. As shown in Fig. 6C, a distinct ECL signal change was observed for ALP (40 U/L), while the interfering enzymes exerted negligible interference even at tenfold higher concentrations, indicating excellent.

The ECL signals of five independent electrodes tested at 40U/L ALP (Fig. 6D) showed a relative standard deviation (RSD) of 3.8%, verifying the good reproducibility of the biosensors. In addition, recovery experiments were conducted by spiking 0.1, 1.0 and 10 U/L ALP in diluted human serum (0.1%). The calculated recoveries were 96.0%, 98.1% and 97.3% with RSDs of 3.2%, 3.3% and 4.0% (Table S7), respectively, revealing the potential application of this biosensor for ALP detection in real biological samples.

4 Conclusion

In this work, the molecule NZ2TPA with HLCT and AIE characteristics was synthesized to dissolve the limitation of luminescence efficiency. The hot exciton molecule exhibits the HLCT state, allowing it to achieve the *h*RISC process from T_2 to S_1 for high utilization of triplet excitons and high luminous efficiency. The presence of AIE greatly enhances the ECL emission of NZ2TPA after reprecipitation, leading to the highest Φ_{ECL} of

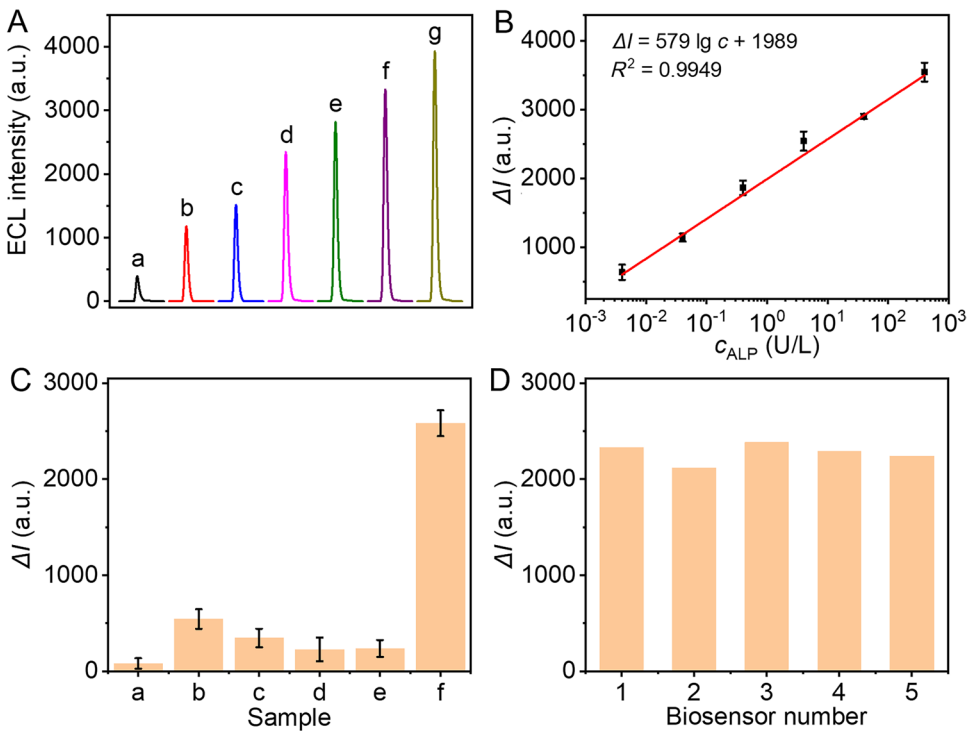

Fig. 6 **A** ECL-time curves of ECL biosensor in 0.1 M PBS pH 7.4 containing 20 mM TPrA at 0, 0.004, 0.04, 0.4, 4, 40, 400 U/L ALP (from a to g). **B** Calibration curve for ALP detection ($n = 3$). **C** Specificity of the biosensor for (a) blank, (b) 400 U/L glucose oxidase, (c) catalase, (d) lysozyme, (e) pepsin and (f) 40 U/L ALP. **D** Reproducibility of five ECL biosensors at 40 U/L ALP

current hot exciton nanomaterials and providing an excellent ECL emitter for constructing sensitive ECL detection methods. Based on the efficient anodic ECL emission of NT NPs, the quenching of MnO_2 NSs on ECL and the reduction of MnO_2 on biosensor surface, a simple "signal-on" method has been proposed for sensitive detection of ALP. The eminent analytical performance with a wide detectable concentration range and low detection limit demonstrates the significant potential of organic nanoemitters with dual functional properties in improving ECL efficiency and expanding the application of hot exciton materials in bioanalysis.

Supplementary Information The online version contains supplementary material available at https://doi.org/10.1007/s41664-025-00374-x.

Acknowledgements This research was funded by by National Natural Science Foundation of China (21890741, 21827812).

Data Availability Data will be available on request.

Declarations

Conflict of Interest The authors declare that they have no conflict of interest.

References

1. Richter MM. Electrochemiluminescence (ECL). Chem Rev. 2004;104(6):3003–36.
2. Miao WJ. Electrogenerated chemiluminescence and its biorelated applications. Chem Rev. 2008;108(7):2506–53.
3. Liu ZY, Qi WJ, Xu GB. Recent advances in electrochemiluminescence. Chem Soc Rev. 2015;44:3117–42.
4. Lei JP, Ju HX. Fundamentals and bioanalytical applications of functional quantum dots as electrogenerated emitters of chemiluminescence. TrAC Trends Anal Chem. 2011;30(8):1351–9.
5. Jia HY, Yang L, Dong X, Zhou LM, Wei Q, Ju HX. Cysteine modification of glutathione-stabilized Au nanoclusters to red-shift and enhance the electrochemiluminescence for sensitive bioanalysis. Anal Chem. 2022;94(4):2313–20.
6. Zhao GH, Dong X, Du Y, Zhang N, Bai GZ, Wu D, Ma HM, Wang YG, Cao W, Wei Q. Enhancing electrochemiluminescence efficiency through introducing atomically dispersed ruthenium in nickel-based metal-organic frameworks. Anal Chem. 2022;94(29):10557–66.
7. Kong LY, Zhao L, Liang HX, Ren X, Ma HM, Liu XJ, Fan DW, Wu D, Wei Q. Self-enhanced biosensor with luminophore-catalyst integrated strategies and ECL-RET for ultrasensitive SARS-CoV-2 N immunoassay. Sens Actuat B Chem. 2025;432: 137478.
8. Li YJ, Cui WR, Jiang QQ, Wu Q, Liang RP, Luo QX, Qiu JD. A general design approach toward covalent organic frameworks for highly efficient electrochemiluminescence. Nat Commun. 2021;12:4735.
9. Wang ZY, Pan JB, Li Q, Zhou Y, Yang S, Xu JJ, Hua DB. Improved AIE-active probe with high sensitivity for accurate uranyl ion monitoring in the wild using portable electrochemiluminescence system for environmental applications. Adv Funct Mater. 2020;30(30):2000220.
10. Doeven EH, Connell TU, Sinha N, Wenger OS, Francis PS. Electrochemiluminescence of a first-row d^6 transition metal complex. Angew Chem Int Ed. 2024;63(21): e202319047.
11. Liu YJ, Zhang HD, Li BX, Liu JW, Jiang DC, Liu BH, Sojic N. Single biomolecule imaging by electrochemiluminescence. J Am Chem Soc. 2021;143(43):17910–4.
12. Valenti G, Rampazzo E, Bonacchi S, Petrizza L, Marcaccio M, Montalti M, Prodi L, Paolucci F. Variable doping induces mechanism swapping in electrogenerated chemiluminescence of $Ru(bpy)_3^{2+}$ core-shell silica nanoparticles. J Am Chem Soc. 2016;138(49):15935–42.
13. Yu SQ, Du Y, Niu XH, Li GM, Zhu D, Yu Q, Zou GZ, Ju HX. Arginine-modified black phosphorus quantum dots with dual excited states for enhanced electrochemiluminescence in bioanalysis. Nat Commun. 2022;13:7302.
14. Li LL, Zhang ZY, Chen Y, Xu Q, Zhang JR, Chen ZX, Chen Y, Zhu JJ. Sustainable and self-enhanced electrochemiluminescent ternary suprastructures derived from $CsPbBr_3$ perovskite quantum dots. Adv Funct Mater. 2019;29(32):1902533.
15. Wu KQ, Zheng YJ, Chen R, Zhou ZX, Liu SQ, Shen YF, Zhang YJ. Advances in electrochemiluminescence luminophores based on small organic molecules for biosensing. Biosens Bioelectron. 2023;223: 115031.
16. Feng YQ, Wang NN, Ju HX. Electrochemiluminescence biosensing and bioimaging with nanomaterials as emitters. Sci China Chem. 2022;65(12):2417–36.
17. Feng YQ, Wang NN, Ju HX. Highly efficient electrochemiluminescence of cyanovinylene-contained polymer dots in aqueous medium and its application in imaging analysis. Anal Chem. 2018;90(2):1202–8.
18. Wang NN, Gao H, Li YZ, Li GM, Chen WW, Jin ZC, Lei JP, Wei Q, Ju HX. Dual intramolecular electron transfer for in situ coreactant-embedded electrochemiluminescence microimaging of membrane protein. Angew Chem Int Ed. 2021;60(1):197–201.
19. Gao H, Lin JB, Wang SM, Tao QQ, Tang BZ, Chen HY, Xu JJ. Near-infrared II aggregation-induced electrochemiluminescence of organic dots. Chem Commun. 2024;60(5):562–5.
20. Liu JX, Ming WJ, Zhang J, Zhou XB, Qin YL, Wu L. Aggregation-induced electrochemiluminescence based on intramolecular charge transfer and twisted molecular conformation for label-free immunoassay. Anal Chim Acta. 2024;1320: 342994.
21. Ishimatsu R, Matsunami S, Kasahara T, Mizuno J, Edura T, Adachi C, Nakano K, Imato T. Electrogenerated chemiluminescence of donor-acceptor molecules with thermally activated delayed fluorescence. Angew Chem Int Ed. 2014;53(27):6993–6.
22. Liu JX, Yang LX, Li SJ, Zhang K, Zhou XB, Li G, Wu L, Qin YL. Near-infrared electrochemiluminescence biosensors facilitated by thermally activated delayed fluorescence (TADF) emitters for ctDNA analysis. Biosens Bioelectron. 2024;251: 116103.
23. Kumar S, Tourneur P, Adsetts JR, Wong MY, Rajamalli P, Chen DY, Lazzaroni R, Viville P, Cordes DB, Slawin AMZ, Olivier Y, Cornil J, Ding ZF, Zysman-Colman E. Photoluminescence and electrochemiluminescence of thermally activated delayed fluorescence (TADF) emitters containing diphenylphosphine chalcogenide-substituted carbazole donors. J Mater Chem C. 2022;10(12):4646–67.
24. Youn Lee S, Yasuda T, Nomura H, Adachi C. High-efficiency organic light-emitting diodes utilizing thermally activated delayed fluorescence from triazine-based donor-acceptor hybrid molecules. Appl Phys Lett. 2012;101(9): 093306.
25. Jia YL, Lin JB, Gao H, Chen HY, Xu JJ. Molecular planar rigidity promoted aggregation-induced delayed electrochemiluminescence of organic dots for nucleic acid assay. Anal Chem. 2024;96(45):18214–20.
26. Wang C, Wu J, Huang H, Xu QQ, Ju HX. Electrochemiluminescence of polymer dots featuring thermally activated delayed

fluorescence for sensitive DNA methylation detection. Anal Chem. 2022;94(45):15695–702.
27. Li WJ, Pan YY, Xiao R, Peng QM, Zhang ST, Ma DG, Li F, Shen FZ, Wang YH, Yang B, Ma YG. Employing ~100% excitons in OLEDs by utilizing a fluorescent molecule with hybridized local and charge-transfer excited state. Adv Funct Mater. 2014;24(11):1609–14.
28. Hu YX, Miao JS, Hua T, Huang ZY, Qi YY, Zou Y, Qiu YT, Xia H, Liu H, Cao XS, Yang CL. Efficient selenium-integrated TADF OLEDs with reduced roll-off. Nat Photon. 2022;16:803–10.
29. Wang C, Cui LJ, Wu J, Hu XF, Wu XT, Cui ZH, Ju HX. Electrochemiluminescence of hot exciton nanomaterial with boosted efficiency for visual bioanalysis. Nano Today. 2024;54: 102131.
30. Li WJ, Liu DD, Shen FZ, Ma DG, Wang ZM, Feng T, Xu YX, Yang B, Ma YG. A twisting donor-acceptor molecule with an intercrossed excited state for highly efficient, deep-blue electroluminescence. Adv Funct Mater. 2012;22(13):2797–803.
31. Yao L, Yang B, Ma YG. Progress in next-generation organic electroluminescent materials: material design beyond exciton statistics. Sci China Chem. 2014;57:335–45.
32. Pan YY, Li WJ, Zhang ST, Yao L, Gu C, Xu H, Yang B, Ma YG. High yields of singlet excitons in organic electroluminescence through two paths of cold and hot excitons. Adv Opt Mater. 2014;2(6):510–5.
33. Xu YW, Xu P, Hu DH, Ma YG. Recent progress in hot exciton materials for organic light-emitting diodes. Chem Soc Rev. 2021;50(2):1030–69.
34. Zhou CJ, Cong DL, Gao Y, Liu HC, Li JY, Zhang ST, Su Q, Wu QL, Yang B. Enhancing the electroluminescent efficiency of acridine-based donor-acceptor materials: quasi-equivalent hybridized local and charge-transfer state. J Phys Chem C. 2018;122(32):18376–82.
35. Zhang L, Wang LZ, Samedov K, Chen MX, Chen DC, Cai YJ. High-lying triplet excitons utilization of silole derivatives enables their efficiency breakthrough in OLEDs. Adv Funct Mater. 2024;34(51):2410250.
36. Liu TX, Zhu LP, Zhong C, Xie GH, Gong SL, Fang JF, Ma DG, Yang CL. Naphthothiadiazole-based near-infrared emitter with a photoluminescence quantum yield of 60% in neat film and external quantum efficiencies of up to 3.9% in nondoped OLEDs. Adv Funct Mater. 2017;27(12):1606384.
37. Wang NN, Feng YQ, Wang YW, Ju HX, Yan F. Electrochemiluminescent imaging for multi-immunoassay sensitized by dual DNA amplification of polymer dot signal. Anal Chem. 2018;90(12):7708–14.
38. Deng RR, Xie XJ, Vendrell M, Chang YT, Liu XG. Intracellular glutathione detection using MnO_2-nanosheet-modified upconversion nanoparticles. J Am Chem Soc. 2011;133(50):20168–71.
39. Kai K, Yoshida Y, Kageyama H, Saito G, Ishigaki T, Furukawa Y, Kawamata J. Room-temperature synthesis of manganese oxide monosheets. J Am Chem Soc. 2008;130(47):15938–43.
40. Balijapalli U, Nagata R, Yamada N, Nakanotani H, Tanaka M, D'Aléo A, Placide V, Mamada M, Tsuchiya Y, Adachi C. Highly efficient near-infrared electrofluorescence from a thermally activated delayed fluorescence molecule. Angew Chem Int Ed. 2021;60(15):8477–82.
41. Wang C, Li XL, Gao Y, Wang L, Zhang ST, Zhao LJ, Lu P, Yang B, Su SJ, Ma YG. Efficient near-infrared (NIR) organic light-emitting diodes based on donor-acceptor architecture: an improved emissive state from mixing to hybridization. Adv Opt Mater. 2017;5(20):1700441.
42. Chaiwai C, Kitisriworaphan W, Petdee S, Nalaoh P, Chawanpunyawat T, Chasing P, Manyum T, Sudyoadsuk T, Promarak V. Solid-state fluorophores featuring a combined hybridized local and charge transfer excited state and aggregation-induced emission as efficient emitters for electroluminescent devices. Dyes Pigm. 2023;216: 111311.
43. Zhang H, Li GG, Guo XM, Zhang K, Zhang B, Guo XC, Li YX, Fan JZ, Wang ZM, Ma DG, Tang BZ. High-performance ultraviolet organic light-emitting diode enabled by high-lying reverse intersystem crossing. Angew Chem Int Ed. 2021;60(41):22241–7.
44. Li WJ, Pan YY, Yao L, Liu HC, Zhang ST, Wang C, Shen FZ, Lu P, Yang B, Ma YG. A hybridized local and charge-transfer excited state for highly efficient fluorescent OLEDs: molecular design, spectral character, and full exciton utilization. Adv Opt Mater. 2014;2(9):892–901.
45. Omer KM, Bard AJ. Electrogenerated chemiluminescence of aromatic hydrocarbon nanoparticles in an aqueous solution. J Phys Chem C. 2009;113(27):11575–8.
46. Feng YQ, Dai CH, Lei JP, Ju HX, Cheng YX. Silole-containing polymer nanodot: an aqueous low-potential electrochemiluminescence emitter for biosensing. Anal Chem. 2016;88(1):845–50.
47. Li JS, Wu TT, Liu XJ, Feng R, Du Y, Li FY, Wei Q. Hexagonal prism-shaped AIE-active MOFs as coreactant-free electrochemiluminescence luminophores coupled with hollow $Cu_{2-x}O$@Pd heterostructures as efficient quenching probes for sensitive biosensing. Anal Chem. 2024;96(45):18170–7.
48. Yang LX, Zhou XB, Zhang K, Liu JX, Zhao LF, Cai AT, Zhao XY, Wu L, Qin YL. Electrochemiluminescent/Electrochemical ratiometric biosensor for extremely specific and ultrasensitive detection of circulating tumor DNA. Sens Actuat B Chem. 2023;382: 133490.
49. Wang C, Tang ZW, Li YR, Li MJ, Xie HJ, Ju HX. Aggregation of thermally activated delayed fluorescence molecules to boost solid electrochemiluminescence efficiency for biosensing of protein-specific glycoforms. Sci China Chem. 2025. https://doi.org/10.1007/s11426-024-2523-2.
50. Zhang X, Ren CH, Hu F, Gao Y, Wang ZY, Li HQ, Liu JF, Liu B, Yang CH. Detection of bacterial alkaline phosphatase activity by enzymatic in situ self-assembly of the AIEgen-peptide conjugate. Anal Chem. 2020;92(7):5185–90.
51. Lu HJ, Xu JJ, Zhou H, Chen HY. Recent advances in electrochemiluminescence resonance energy transfer for bioanalysis: fundamentals and applications. TrAC Trends Anal Chem. 2020;122: 115746.
52. Li H, Wang ZY, Zhao JY, Guan YW, Liu YY. Dual colorimetric and ratiometric fluorescent responses for the determination of glutathione based on fluorescence quenching and oxidase-like activity of MnO_2 nanosheets. ACS Sustain Chem Eng. 2020;8(43):16136–42.
53. Nie YX, Liang ZH, Wang PL, Ma Q, Su XG. MXene-derived quantum dot@gold nanobones heterostructure-based electrochemiluminescence sensor for triple-negative breast cancer diagnosis. Anal Chem. 2021;93(51):17086–93.